Catalysis Letters (2018) 148:3701–3714
https://doi.org/10.1007/s10562-018-2569-z

Facile Synthesis of Ag–γ-Fe_2O_3 Superior Nanocomposite for Catalytic Reduction of Nitroaromatic Compounds and Catalytic Degradation of Methyl Orange

S. A. Sallam[1] · G. M. El-Subruiti[1] · A. S. Eltaweil[1]

Received: 1 July 2018 / Accepted: 23 September 2018 / Published online: 5 October 2018

Abstract

A facile synthetic route for preparing silver-doped maghemite (Ag–γ-Fe_2O_3) nanocomposite via a modified co-precipitation method was developed. The prepared magnetic nanocomposite was characterized by means of thermal analysis, transmission electron microscope, X-Ray diffraction, vibrating sample magnetometer and Fourier transform infrared techniques. The characterization results showed that the prepared Ag–γ-Fe_2O_3 nanocomposite is nanocrystalline and 6–8 nm in size with superparamagnetic behavior. The synthesized Ag–γ-Fe_2O_3 nanocomposite showed exceptional catalytic activities towards reduction of nitroaromatic compounds with specific activities parameters of 1441.7 and 904.2 s^{-1} $g_{Ag}{}^{-1}$ for both 4-nitrophenol and 2-nitroaniline, respectively. Besides, it shows a superior activity for catalytic degradation of methyl orange. All the three catalytic reactions were carried out in aqueous medium at room temperature and in the presence of reducing agent $NaBH_4$. The magnetic behavior of the synthesized Ag–γ-Fe_2O_3 enables the ease of separation of the nanocomposite from the reaction medium for further reuse.

Graphical Abstract

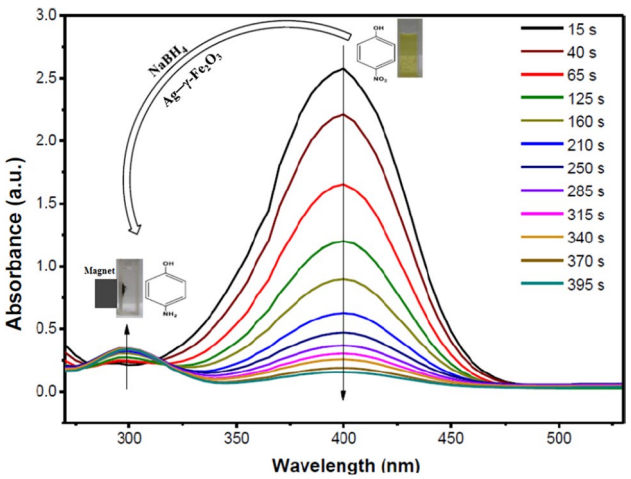

Keywords 4-NP · Magnetic · Degradation · Silver · Nanocomposite

1 Introduction

In the last few decades, public health and environmental safety have been paid much attention [1–3]. Chemical contamination of surface water represents a great risk on the

✉ A. S. Eltaweil
abdelazeemeltaweil@alexu.edu.eg

[1] Chemistry Department, Faculty of Science, Alexandria University, Alexandria, Egypt

aquatic environment. A major reason of this contamination is the disposal of nitroaromatic compounds (NACs), as well as dyes [1, 2]. NACs have been vastly used in many industrial and agricultural fields, such as polymers, pharmaceuticals, intermediates synthesis of dye, and pesticides [4–6]. p-nitrophenol (4-NP) and o-nitroaniline (2-NA) are durable aromatic contaminants discharged from various industries such as dyes, explosives, pesticides, plasticizers and herbicides [7, 8]. Nitrophenol and nitroaniline and their derivatives are highly toxic even at extremely low levels [9], particularly for green plants and for aquatic organisms in surface waters [10]. Moreover, even traces of 2-NA in aquatic environment is harmful to human health and it is a potentially carcinogenic and mutagenic [11, 12]. Therefore, the United States Environmental Protection Agency has reported both nitrophenols and NACs as dangerous and high priority contaminants. Subsequently, a great challenge for chemists is to improve the methods of NACs removal [13].

Another major cause for environmental concern is the presence of dyes in water [14]. Mostly, dyes are highly stable and synthesized to resist the degradation, which makes their remediation a great challenge for chemists. Azo dyes represents about a half of synthetic textile dyes production, and about 15% of these dyes disposes in wastewaters during the dyeing processes [15]. Azo dyes are stable under aerobic treatments. For this reason, catalytic and photocatalytic degradation treatment of azo dye wastewaters received much attention recently [16, 17].

Recently, magnetic nanoparticles have been gained much interest, because of their wide range applications including magnetic ferrofluids [18], catalysis [19], energy storage [20], information storage spintronics [21] and bioseparations [22]. Furthermore, due to their biocompatibility and non-toxicity to humans [23, 24], they are widely used in biomedicine applications such as making the quality of magnetic resonance imaging (MRI) more efficient, drug delivery and also in manipulating cell membranes biomedicine [25–27]. Among most common forms of iron oxides, maghemite (γ-Fe_2O_3) is greatly applicable in medical and industrial applications [28]. It has been reported that doping of nanocrystalline γ-Fe_2O_3 with suitable doping metals greatly improves their properties by narrowing the energy-band gap and inhibiting electron–hole recombination [29]. Furthermore, it also can improve its activity as well as selectivity [30, 31]. Doping γ-Fe_2O_3 with a metal could be resulted in a greater catalytic activity compared with un-doped γ-Fe_2O_3 [32].

Taking into account all these considerations, the present work aimed to develop a facile, easily separable and highly efficient nanocomposite for the catalytic reduction of NACs as well as azo dyes. Thus, in this work, maghemite was used as a magnetic support to stabilize non-toxic Ag nanoparticles to obtain Ag–γ-Fe_2O_3 nanocomposite with exceptional activity, superparamagnetic behavior and excellent reusability in the catalytic reactions.

2 Materials and Methods

2.1 Materials

Ferrous sulphate heptahydrate ($FeSO_4 \cdot 7H_2O$) was purchased from Merck. Analytical grade ferric chloride hexahydrate ($FeCl_3 \cdot 6H_2O$), silver nitrate ($AgNO_3$), sodium borohydride ($NaBH_4$), and hydrochloric acid (HCl) were purchased from Sigma-Aldrich. All chemicals and solvents used in the synthesis processes were used as received without any further purification.

2.2 Synthesis of Maghemite Nanoparticles (γ-Fe_2O_3)

γ-Fe_2O_3 nanocomposite, was prepared according Chakrabarti et al. method [8] with some modifications. In this method salts of both ferrous and ferric ions were used. $FeSO_4 \cdot 7H_2O$ was the precursor of Fe^{2+} ions, while $FeCl_3 \cdot 6H_2O$ was the precursor of Fe^{3+} ions. $FeSO_4 \cdot 7H_2O$ (0.70 g) and $FeCl_3 \cdot 6H_2O$ (1.35 g) were dissolved in 50 ml distilled water under inert atmosphere and stirred for 30 min, and then NH_4OH solution (25%) was added to the aqueous solution of Fe^{2+} and Fe^{3} ions dropwise under vigorous stirring, until pH reaches about ~ 9.5. Instant black precipitate of Fe_3O_4 was obtained. This precipitate was acidified to pH ~ 2 to 3 by adding hydrochloric acid (6 M). After acidification process, the black precipitate was turned into a chocolate brown precipitate, indicating the formation of γ-Fe_2O_3 nanoparticles [8]. The resulted magnetic nanocomposite was stirred for another 1 h, collected by an external magnet, washed several times with distilled water and ethanol and finally dried in oven at 200 °C for 3 h.

2.3 Synthesis of Silver-Doped Maghemite Nanocomposite (Ag–γ-Fe_2O_3)

Previously prepared γ-Fe_2O_3 (0.50 g) was dispersed in 50 ml deionized water and sonicated for 30 min, then $AgNO_3$ aqueous solution (10 ml, 0.042 g) was added dropwise under stirring, then freshly prepared $NaBH_4$ aqueous solution (10 ml, 0.019 g) was added dropwise to the suspension (in order to reduce Ag^+ ions), and the mixture was sonicated for 1 h. The formed silver doped maghemite (Ag–γ-Fe_2O_3) nanocomposite was collected by an external magnet, washed with deionized water and ether, then dried under vacuum at 50 °C for 6 h.

2.4 Catalytic Activity Experiments

2.4.1 Reduction of NACs Experiment

In catalytic reduction of 4-NP experiment, freshly prepared aqueous $NaBH_4$ solution (0.5 ml, 0.2 M) was added to aqueous 4-NP solution (2 ml, 0.12 mM). Upon the addition of $NaBH_4$ the yellow solution of 4-NP turned into deep yellow solution indicating the formation of 4-nitrophenolate [13]. Subsequently, Ag–γ-Fe_2O_3 nanocomposite (100 µl, 1 mg ml^{-1}) was added to the deep yellow mixture which turned colorless at the end of the reaction. To examine the reusability of Ag–γ-Fe_2O_3 nanocomposite, the used nanocomposite was separated from the reaction mixture using an external magnet after the completion of the reaction. The recovered nanocomposite was washed with ethanol and water repeatedly for the subsequent use. Reduction process of 4-NP was repeated twelve times using the recycled nanocomposite.

Similarly, in catalytic reduction of 2-NA experiment, freshly prepared aqueous $NaBH_4$ solution (0.5 ml, 0.2 M) was added to aqueous solution of 2-NA (2 ml, 0.12 mM), and then Ag–γ-Fe_2O_3 nanocomposite (100 µl, 1 mg ml^{-1}) was added to the mixture. The yellow colored solution of 2-NA became colorless, confirming the reduction of 2-NA. For the two catalytic reduction reactions, the temperature was kept at 25 °C.

2.4.2 Catalytic Degradation of Methyl Orange

In catalytic degradation of methyl orange (MO) experiment, 2 ml of 0.5 M aqueous $NaBH_4$ solution was added to 20 ml of MO solution (100 mg l^{-1}), and then nanocomposite (1 mg) was added while stirring. The color of MO vanished gradually, indicating the catalytic degradation of MO. The temperature of the process was kept at 25 °C. UV–Vis absorption spectra technique was used to monitor all of the three reactions.

2.5 Characterization

Thermogravimetric analysis (TG) was carried out using a Linseis STA PT-1000. The rate of heating was 10 °C min^{-1}. The morphology and particles size were determined using transmission electron microscope (JEOL, JEM 100 CX, Japan). Crystal phase and crystallite size are obtained by X-ray diffractometer (XRD BRUKER D8 Advance Cu target, Germany), operating with CuKα radiation (λ = 1.54 Å) generated at 40 KV and 40 mA. Scans are performed for 2θ values between 10° and 80° with a 2θ step of 0.02 for 0.4 s per point. Room temperature magnetic characteristics of Ag–γ-Fe_2O_3 were determined by using a vibrating sample magnetometer (VSM) in an external magnetic field of 20 KG (20 KOe). The FT-IR spectra of the magnetic nanocomposite were taken in potassium bromide disc using Perkin Elmer spectrophotometer (Model 1430) covering frequency range 400–4000 cm^{-1}. The instrument was calibrated by a polystyrene film (1602 ± 1 cm^{-1}). UV–Vis absorption spectra were monitored by a PG-spectrophotometer instrument.

3 Results and Disucssion

3.1 Catalyst Characterization

The total mass loss was evaluated to be ~ 13.5% according to the TG analysis up to 600 °C, as shown in Fig. 1.

The TG curve for Ag–γ-Fe_2O_3 is shown in Fig. 1. In the TG curve, the mass loss by dehydration of physically adsorbed water molecules from the catalyst surface

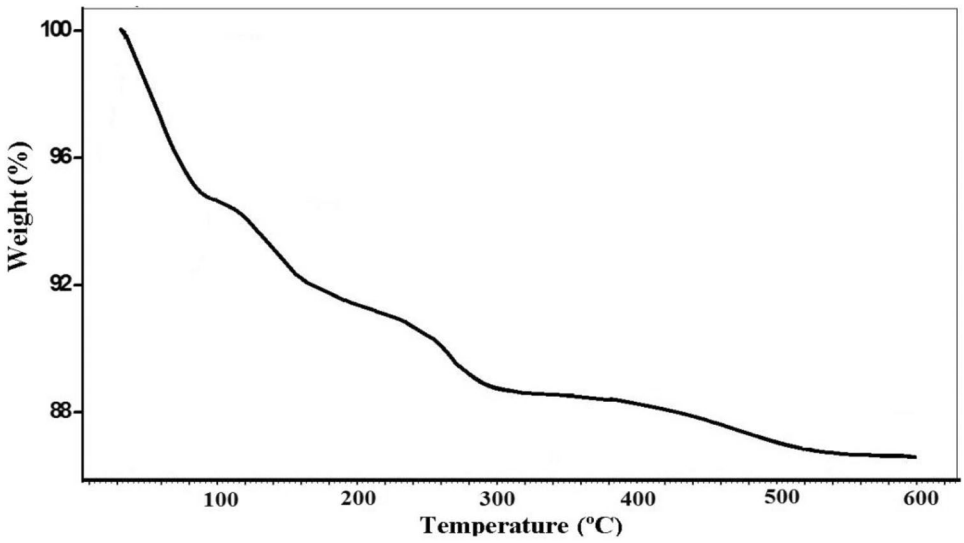

Fig. 1 The TG curve of Ag–γ-Fe_2O_3 nanocomposite

was observed at ~ 100 °C. This was evaluated to be 5.5% according to the TG analysis, then the sample mass gradually decreased (3.6%) at higher temperatures up to 180 °C which is due to chemically adsorbed water [33]. Additionally, TG curve shows small losses in two consecutive steps, firstly between 220 °C and 300 °C (2.7%) is due to the complete transition of Fe_3O_4 to γ-Fe_2O_3, while the other loss between 420 and 540 °C (2%) is due to the transition of γ-Fe_2O_3 into α-Fe_2O_3 [34]. The total mass loss was evaluated to be ~ 13.5% according to the TG analysis up to 600 °C, as shown in Fig. 1.

It may be observed from TEM Fig. 2a–c that, the as-synthesized γ-Fe_2O_3 nanoparticles and Ag–γ-Fe_2O_3 nanocomposite are spherical in shape with nano-dimensions ranging from 4 to 6 nm for pure γ-Fe_2O_3 and from 6 to 10 nm for Ag–γ-Fe_2O_3. TEM micrograph showed that doping maghemite with Ag increased the agglomeration of the particles.

The crystallinity of Ag–γ-Fe_2O_3 nanocomposite was examined by XRD study as shown in Fig. 3. The diffractogram fits very well with the cubic symmetry (space group P4132) of γ-Fe_2O_3 (Card No. 039-1346). In addition, the obtained lattice parameters a = b = c = 8.3565 Å and the sharp characteristics of the peaks confirm the presence of the cubic structure and good crystallinity [35]. Diffraction peaks at around 2θ = 30.4°, 35.6°, 43.3°, 53.7°, 57.2°, and 63.1° corresponding to the (220, 311, 400, 422, 511, and 440) planes respectively, have been assigned to a spinel structure with characteristics of maghemite [8], while the diffraction peaks of silver at 2θ = 38.1°, 44.6°, 64.7°, and 77.5° corresponding to the (111, 200, 220 and 311) planes identify the sample as a face-centered cubic lattice of Ag (space group Fm-3m No. 225) with cell constants of a = 4.074 Å (JCPDS Card File No. 003-0921) [12].

The magnetic property of Ag–γ-Fe_2O_3 nanocomposite was characterized by VSM. Figure 4 shows a typical room temperature magnetization curve of Ag–γ-Fe_2O_3 nanocomposite. The M_s (saturation magnetization) of Ag–γ-Fe_2O_3 nanocomposite as shown from the magnetization curve is 63.76 emu g^{-1}. This value is slightly less than the value of pure γ-Fe_2O_3 nanoparticles (65.24 emu g^{-1}), due to the introduction of non-magnetic silver nanoparticles. Our results showed that the H_c of nanocomposite

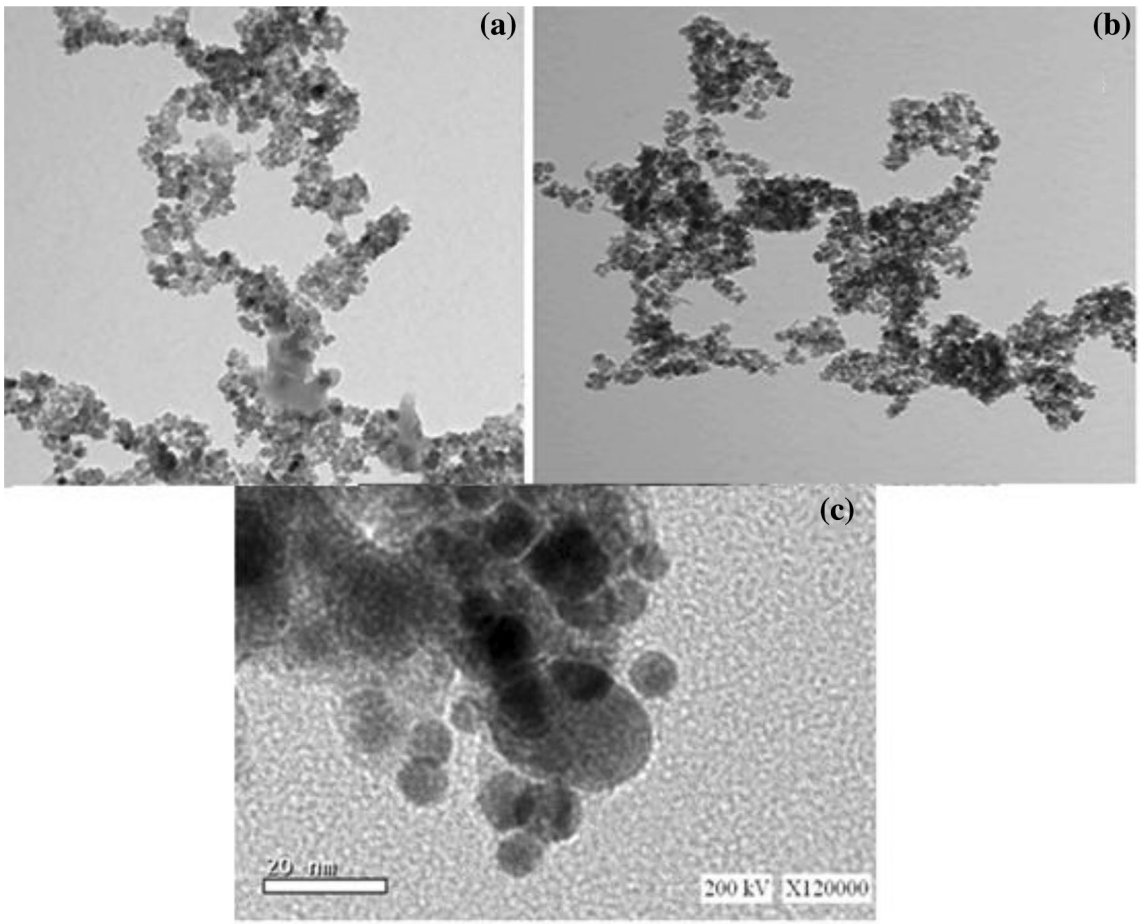

Fig. 2 TEM of pure γ-Fe_2O_3 nanoparticles (**a**), TEM of Ag–γ-Fe_2O_3 nanocomposite (**b**), HTEM of Ag–γ-Fe_2O_3 nanocomposite (**c**)

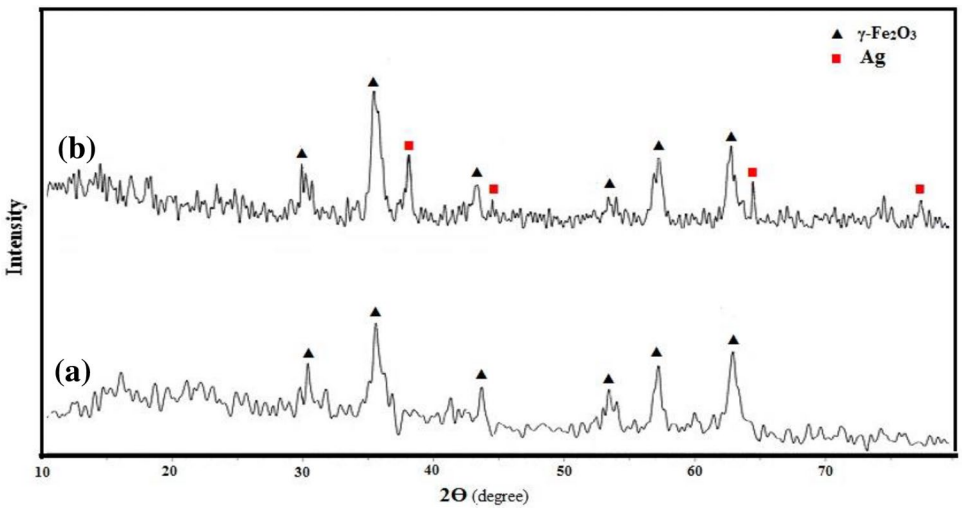

Fig. 3 The X-ray diffraction pattern of: (a) pure γ-Fe_2O_3 nanoparticles, (b) Ag–γ-Fe_2O_3 nanocomposite

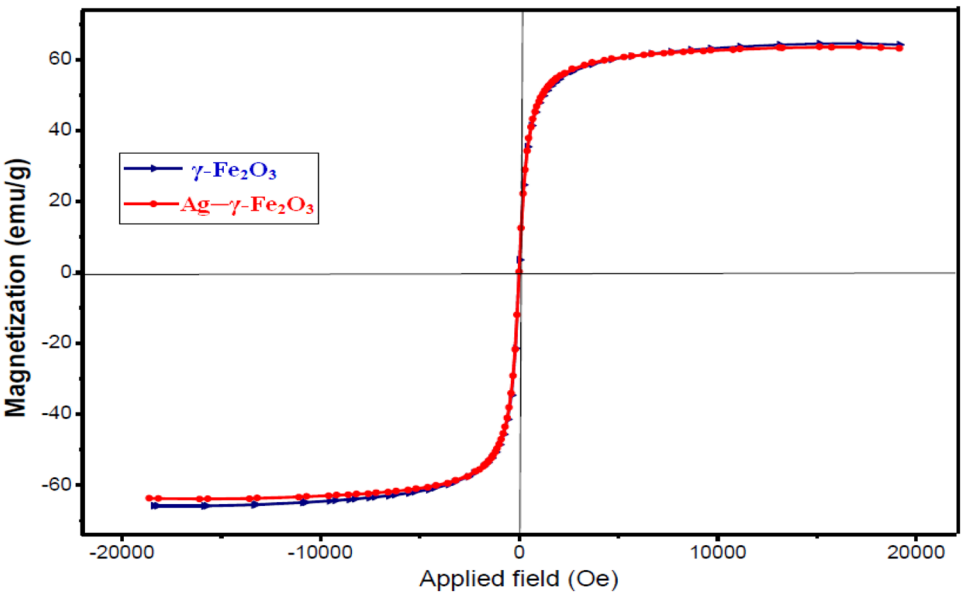

Fig. 4 The hysteresis loop of pure γ-Fe_2O_3 nanoparticles and Ag–γ-Fe_2O_3 nanocomposite at room temperature

approaches zero confirming the supermagnetic behavior of the nanocomposite with M_r (remanent magnetization) of 1.0025 emu g^{-1}.

FT-IR spectra of γ-Fe_2O_3 nanoparticles and Ag–γ-Fe_2O_3 nanocomposite are shown in Fig. 5. It is obvious that Ag–γ-Fe_2O_3 has similar spectrum to that pure γ-Fe_2O_3. However, the two peaks at 560 and 630 cm^{-1} observed in case of pure γ-Fe_2O_3 which related to the Fe–O group were replaced by a new peak at 578 cm^{-1} upon doping γ-Fe_2O_3 with Ag. The adsorbed water shows a broad band between 3430 and 3440 cm^{-1} assigned to O–H stretching in H-bonded water and bands located at 1633 in pure γ-Fe_2O_3 and at 1640 cm^{-1} in Ag–γ-Fe_2O_3 are due to the O–H bending vibration of molecular water [11]. Moreover, no peaks were observed for silver nanocomposite. This is mainly because silver nanocomposite do not have absorption in the Infrared region [36].

Figure 6a, b represents the UV–Visible spectra of pure γ-Fe_2O_3 and Ag–γ-Fe_2O_3, respectively. The intensity of absorption for the samples increased with decreasing wavelength as expected for nanomaterials [37]. Tauc's relationship was used calculate the energy gap as follows: $\alpha h\nu = A(h\nu - E_g)^2$, Where α is the absorption coefficient, A is a constant, h is Planck's constant. The extrapolation of the linear region of a plot of $(ah\nu)^2$ versus hν, gives the value of the band gap of the samples. The energy gap was found to be 2.14 eV for Ag–γ-Fe_2O_3 and 2.59 eV for pure γ-Fe_2O_3 which is in good agreement with a energy gap value of 2.65 eV for Fe_2O_3 [38].

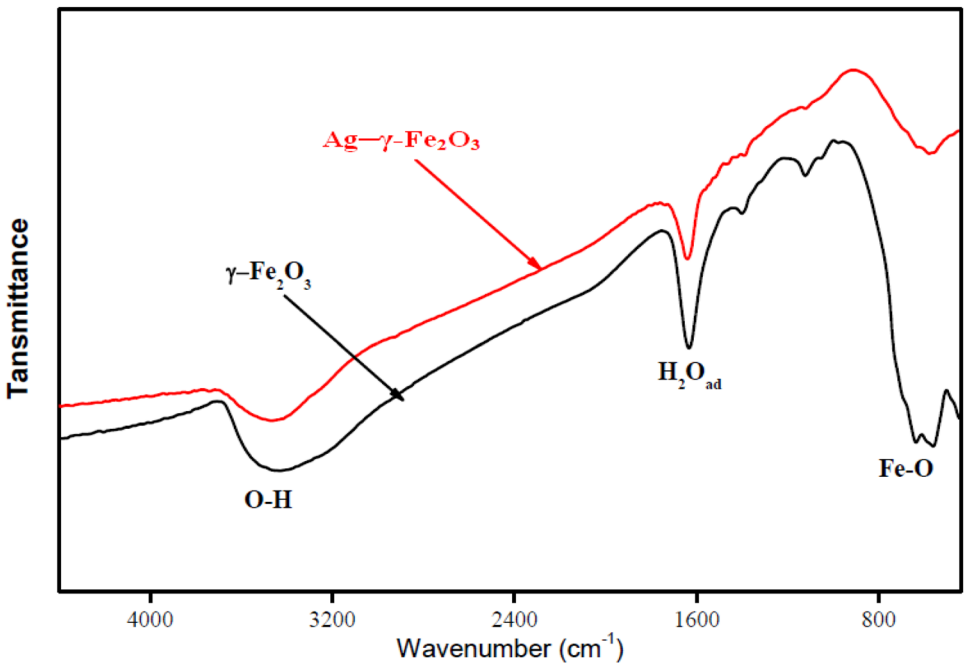

Fig. 5 The FT-IR spectra of pure γ-Fe_2O_3 nanoparticles and Ag–γ-Fe_2O_3 nanocomposite

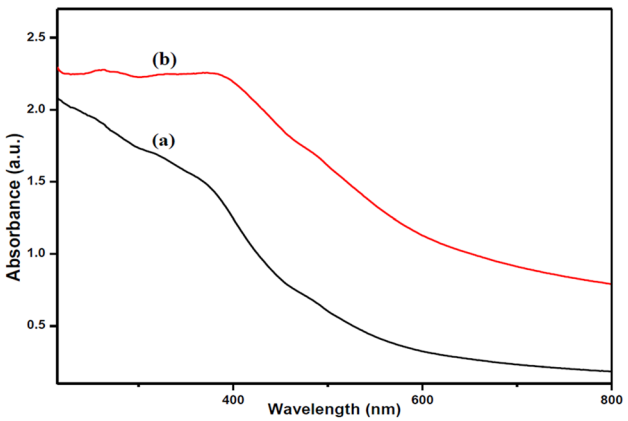

Fig. 6 Variation of absorption coefficient of pure γ-Fe_2O_3 nanoparticles (a) and Ag–γ-Fe_2O_3 nanocomposite (b)

3.2 Catalytic Tests

3.2.1 Reduction of Nitroaromatic Compounds

Ag–γ-Fe_2O_3 nanocatalyst was tested in the reduction of NACs (4-NP and 2-NA). Both reduction reactions of 4-NP and 2-NA were followed by measuring the change in UV–Vis absorbance using spectrophotometry technique since a single product is resulted in each reaction [39, 40]. Furthermore, the reduction reaction of 4-NP was selected to investigate the reusability as well as the activity of the synthesized Ag–γ-Fe_2O_3 nanocomposite.

4-NP has a specific λ_{max} at 317 nm which is shifted to 400 nm upon addition of aqueous $NaBH_4$ solution, indicating the formation of the corresponding phenolate ions [13, 41, 42]. This λ_{max} at 400 nm corresponding to p-nitrophenolate ions did not change over time (2 days) in absence of the nanocatalyst affirming that the reaction did not proceed by aqueous $NaBH_4$ solution. Furthermore, when γ-Fe_2O_3 nanoparticles (100 mg) were added to 4-NP and $NaBH_4$ mixed solution, it takes more than 2 h to be 5% completed (results not shown here). However, the addition of 1 mg of Ag–γ-Fe_2O_3 nanocatalyst to a mixture of 4-NP and freshly prepared $NaBH_4$, led to a quick decrease in the peak intensity at 400 nm, while another peak at 300 nm (assigned to 4-aminophenol) increased (Fig. 7a) indicating the reaction progress. On the other hand, 2-NA has two distinct absorption peaks located at 410 nm and 285 nm [13] with no apparent change in the position of the two peaks upon the addition of $NaBH_4$. Addition of pure γ-Fe_2O_3 (100 mg) to 2-NA and $NaBH_4$ mixed solution showed no change in the peaks intensities. However, the addition of 1 mg of Ag–γ-Fe_2O_3 to a mixture of 2-NA and freshly prepared $NaBH_4$, led to an instant decrease in the peaks intensities at 410 nm and 285 nm (Fig. 7b) confirming the reduction of 2-NA.

Catalytic reduction of the 4-NP and 2-NA to the corresponding amino compound (Scheme 1) in the presence of Ag–γ-Fe_2O_3 were completed in 6 and 10 min, respectively. For the reduction process to be occur, NACs and borohydride ions were adsorbed on Ag–γ-Fe_2O_3 and an electron relaying from the borohydride ions to the NACs ions [43].

Both reactions were adjusted to be first order, by taking $NaBH_4$ in much higher concentration than those of nitro compound and can be considered as a constant during the

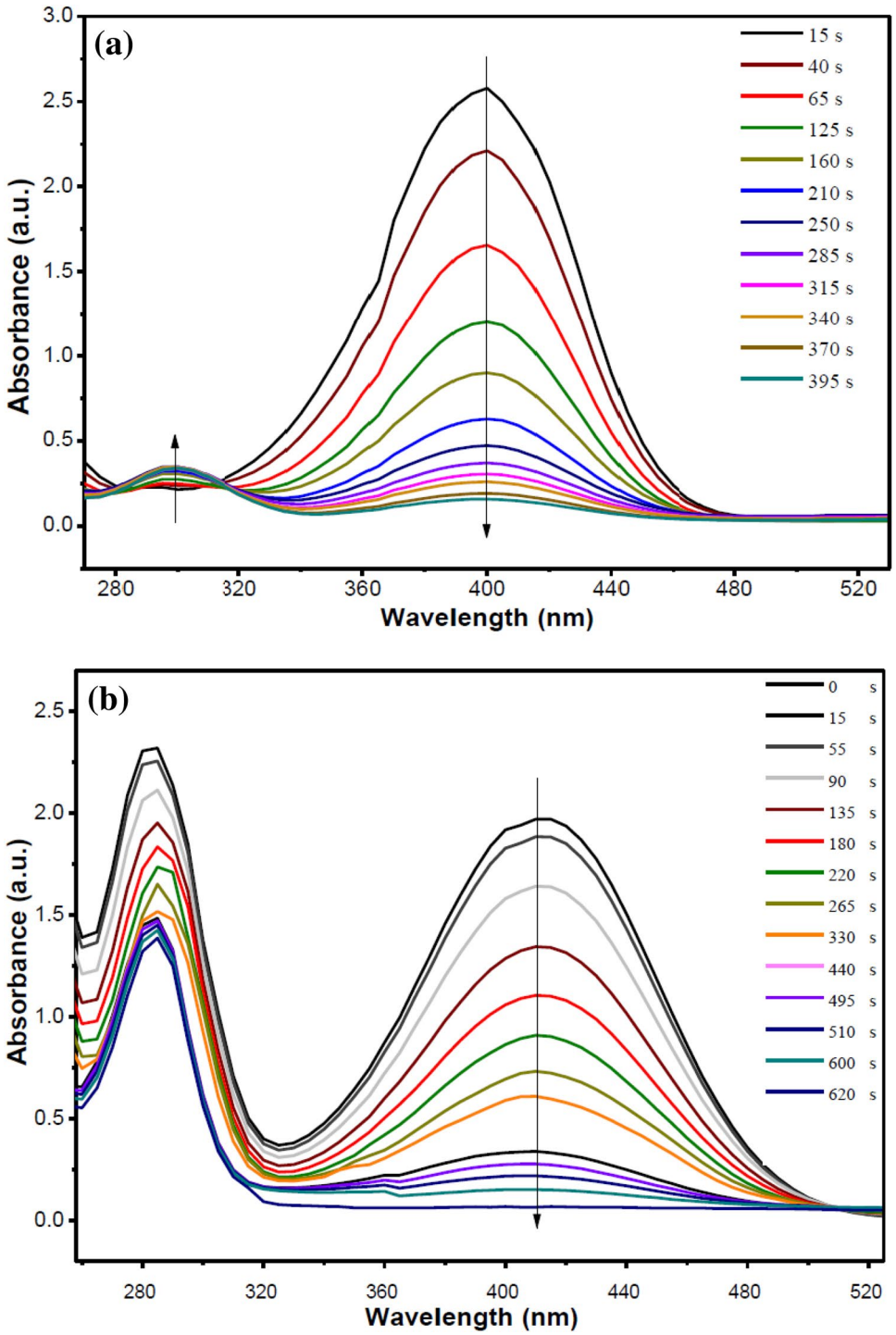

Fig. 7 The UV–Vis spectra for: reduction of 4-NP to 4-AP (**a**), reduction of 2-NA to o-PDA (**b**), over Ag–γ-Fe_2O_3 nanocomposite

reaction period. The first order kinetic equation can be expressed as:

$$\ln\left(C_t/C_0\right) = -kt \quad (1)$$

where; C_o, C_t are the concentration of NACs at reaction time zero and t, respectively and k is the observed first-order rate constant (s^{-1}), t is the reaction time (s).

Figure 8 represents the plots of (C_t/C_0) and ln (C_t/C_0) for reduction of NACs against reaction time (s) in the presence of Ag–γ-Fe_2O_3 at 25 °C. The linear relationship of ln (C_t/C_o) versus reaction time (t) indicates that both reduction reactions follow the pseudo first-order kinetics with respect to NACs concentrations. The specific rate constants

Scheme 1 Reduction of NACs to the corresponding amino compounds over Ag–γ-Fe_2O_3 nanocomposite

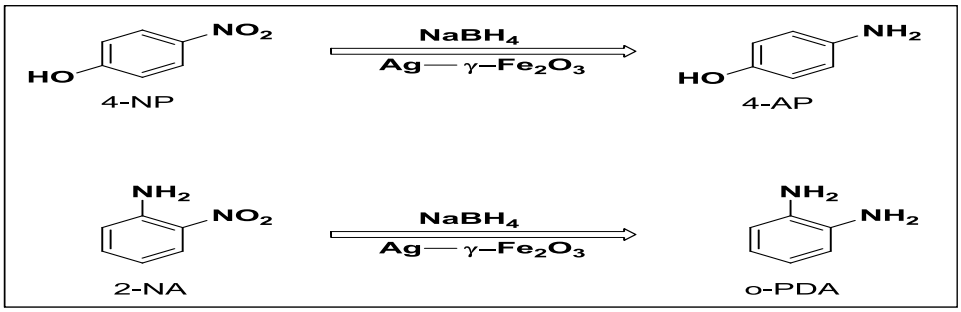

Fig. 8 Plots of: (C_t/C_0) and ln(C_t/C_0) versus reaction time for reduction of 4-NP and 2-NA in the presence of Ag–γ-Fe_2O_3 nanocomposite at 25 °C

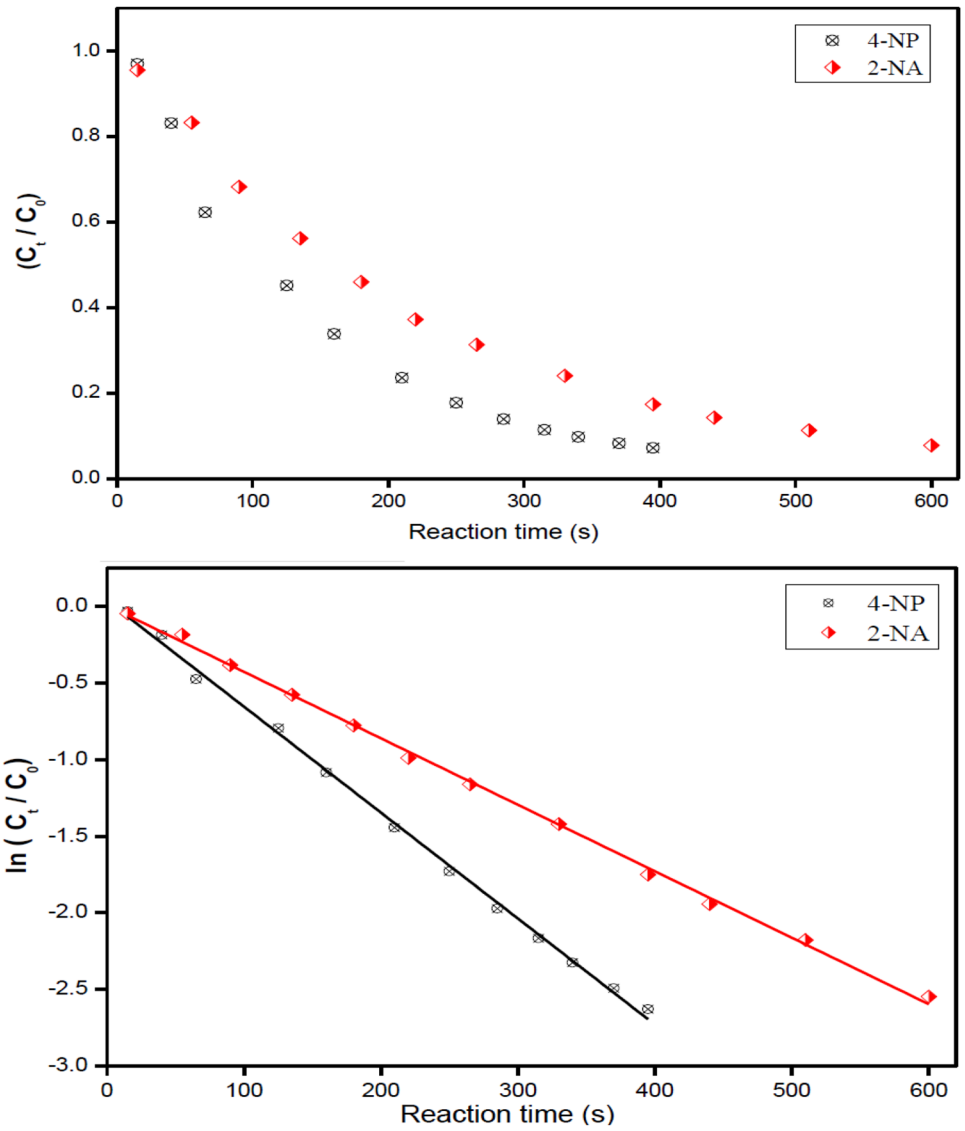

were calculated to be 6.92×10^{-3} s^{-1} and 4.34×10^{-3} s^{-1} for reduction of 4-NP and 2-NA, respectively. Table 1 shows a comparison of the results of Ag–γ-Fe_2O_3 with the literature already reported for catalytic reduction of NACs [44, 45]. The superior catalytic activity of Ag–γ-Fe_2O_3 nanocomposite may be due to high dispersion of Ag on magnetic based material with enhanced activity. Besides, the magnetic behavior of Ag–γ-Fe_2O_3 adds another advantage for its ease separation and reuse.

The activity parameter k′ (k/M, where M is the total mass of the whole catalyst used) was investigated for Ag–γ-Fe_2O_3 nanocomposite. Table 1 shows the comparative results of

Table 1 Comparison of rate constant and activity parameter of Ag–γ-Fe_2O_3 nanocomposite for reduction of NACs with reported catalysts

Catalyst	Rate constant k (s^{-1})	Activity parameter k/M (s^{-1} g^{-1})	References	Compound
Pt(0)/3-ampy-RGO	1.11×10^{-3}	2.76	[44]	4-NP
[Pt(ppy)Cl(3-ampy)]/GO	2.04×10^{-3}	5.10	[44]	4-NP
p(AMPS)-Ni	9.38×10^{-4}	0.019	[46]	4-NP
p(AMPS)-Cu	1.72×10^{-3}	0.172	[47]	4-NP
p(AMPS)-Co	2×10^{-3}	0.04	[48]	4-NP
Ag–Fe_2O_3–C nanoparticles	1.10×10^{-3}	0.022	[49]	4-NP
Ag/C spheres	1.69×10^{-3}	1.69	[50]	4-NP
TAC-Ag-1.0	5.19×10^{-3}	1.30	[51]	4-NP
Ag@PEI@AHB nanoparticles	1.93×10^{-2}	0.48	[52]	2-NA
Au/Co_3O_4 NCs	5.00×10^{-3}	33.3	[53]	2-NA
Ag/KCC-1	4.30×10^{-3}	14.3	[13]	2-NA
Ag/KCC-1	1×10^{-2}	50.0	[13]	3-NA
Ag–γ-Fe_2O_3	6.92×10^{-3}	69.2	This work	4-NP
Ag–γ-Fe_2O_3	4.34×10^{-3}	43.4	This work	2-NA

Ag–γ-Fe_2O_3 with the other catalysts reported for catalytic reduction of 4-NP and 2-NA. The activity parameters for the reduction of both 4-NP and 2-NA by Ag–γ-Fe_2O_3 nanocomposite were found to be 69.2, and 43.4 s^{-1} $g_{cat}{}^{-1}$, respectively. The activity parameters values of Ag–γ-Fe_2O_3 nanocomposite for both reactions are significantly higher than the reported catalysts [13, 44, 46–53], reflecting the superior activity of Ag–γ-Fe_2O_3 nanocomposite towards the reductions of NACs.

Because of their importance reusability and activity of Ag–γ-Fe_2O_3 were investigated. The activity was estimated based on the decrease of the rate of each cycle compared to the rate of first cycle. At the end of the reaction of 4-NP, Ag–γ-Fe_2O_3 nanocomposite was recovered by using an external magnet and washed with water and ethanol several times for further reuses. Figure 9 shows that the reaction is completed each time using the recovered Ag–γ-Fe_2O_3 nanocomposite. Ag–γ-Fe_2O_3 nanocomposite was recycled for twelve cycles for the 4-NP reaction with a transformation of about 98% during 6 min. On the other hand, the activity of the Ag–γ-Fe_2O_3 nanocomposite slightly decreased to 96% at the twelfth cycle.

However, the actual catalyst in the as-synthesized composite is the Ag nanoparticles, since γ-Fe_2O_3 has negligible activity toward the NACs reduction reactions. A normalized activity parameter named specific activity parameter k

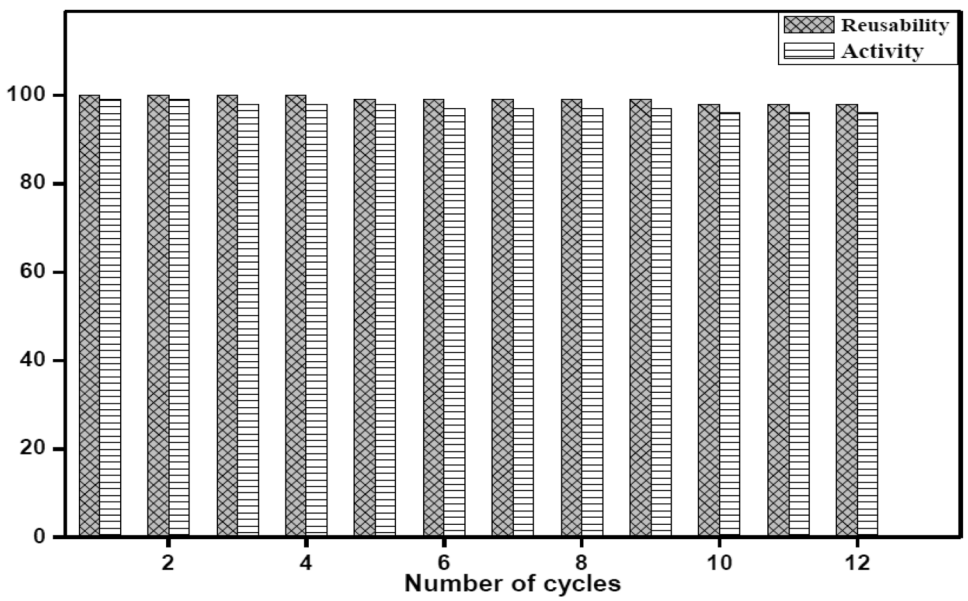

Fig. 9 The reusability and activity of Ag–γ-Fe_2O_3 nanocomposite for the reduction of 4-NP of 25 °C

(k/M′, where M′ is the mass of the Ag in the catalyst used) was calculated and compared to other Ag-based catalysts reported for the reduction of 4-NP as a model reaction (Table 2). Hence, if the amount of Ag loading (4.8%) is considered, the specific activity parameter k is calculated for Ag–γ-Fe_2O_3 to be 1441.7 and 904.2 s^{-1} $g_{Ag}{}^{-1}$ for both 4-NP and 2-NA respectively, which are exceptionally high as compared to the values reported in the literature. It is obvious from Table 2 that the as-synthesized Ag–γ-Fe_2O_3 nanocomposite possesses a significantly much higher (2.6–1442 times) specific activity parameter than other reported Ag-based catalysts [13, 36, 54–59]. Moreover, the as-prepared Ag–γ-Fe_2O_3 nanocomposite can be recovered and reused easily and successfully for at least twelve times with a conversation rate higher than 98%, indicating the Ag–γ-Fe_2O_3 with much higher activities, as well as more reusability than other Ag-based catalysts including the magnetic based towards the reduction of 4-NP. Moreover, the as-synthesized Ag–γ-Fe_2O_3 nanocomposite showed much enhanced activity and reusability in the reduction of NACs compared to the reported magnetic-based silver catalysts Ag-Fe_2O_3 microboxes [54], Ag-Fe_2O_3 [55], Fe_3O_4@SiO_2–Ag [56] and Fe_3O_4@SiO_2–Ag [36]. These results reflect that our synthetic route of Ag–γ-Fe_2O_3 is greatly optimize the activity of silver nanoparticles with retention of superparamagnetic magnetic behavior of γ-Fe_2O_3.

3.2.2 Catalytic Degradation of Methyl Orange

According to literature the degradation of MO by $NaBH_4$ in absence of a catalyst is thermodynamically favorable, but it is kinetically difficult [60]. This can be altered using metal nanocomposite which provides an alternative pathway with lower activation energy. The magnetic Ag–γ-Fe_2O_3nanocomposite was used as catalysts for the catalytic degradation of MO by $NaBH_4$. The kinetics of the catalytic degradation of MO was followed by measuring the absorbance of samples at specific λ_{max} = 465 nm at different time intervals as shown in Fig. 10. The catalytic degradation reaction was adjusted to be first order with respect to MO, and the degradation rate can be easily calculated from the absorbance at 465 nm at different time intervals. When degradation reaction proceeded the absorption peak at 465 nm was gradually decrease with time and the solution turned colorless, confirming complete degradation of the dye [61].

Catalytic degradation of MO with $NaBH_4$ did not proceed in absence of catalyst or even in the presence of pure γ-Fe_2O_3 (2 days). However, addition of 1 mg of Ag–γ-Fe_2O_3 to a mixture of MO (20 ml, 100 mg/l) and freshly prepared $NaBH_4$ (2 ml, 0.5 M) led to an instant decrease in the peak intensity at 465 nm corresponding to MO as shown in Fig. 10. Results showed that Ag–γ-Fe_2O_3has high activity towards catalytic degradation of MO, where it takes ~ 30 min. to be 100% decomposed.

In a similar manner to NACs reduction reactions, the pseudo first-order kinetics applied and the rate constants for the catalytic degradation of MO was calculated. Plot of $\ln(C_t/C_o)$ versus reaction time (Fig. 11) confirm the pseudo-first order kinetics for catalytic degradation of MO. Figure 11 represents plots of (C_t/C_0) and $\ln(C_t/C_0)$ for degradation of MO against reaction time (s), respectively. Plot of $\ln(C_t/C_0)$ showed that the degradation reaction is first order with specific rate constant $k = 1.53 \times 10^{-3}$ s^{-1}. Table 3 shows a comparison of the results of Ag–γ-Fe_2O_3 with the literature already reported for catalytic degradation of MO. Our synthesized Ag–γ-Fe_2O_3 nanocomposite has efficiency ≥ 99% in

Table 2 Comparison of specific activity of Ag–γ-Fe_2O_3 nanocomposite for the reduction of 4-NP as a model reaction with reported Ag-based catalysts

Catalyst	Mass of catalyst	Metal(s) loading (wt%)	k (s^{-1})	$k' = k/M^a$ (s^{-1} $g_{cat}{}^{-1}$)	$k = k/M^b$ (s^{-1} $g_{metal}{}^{-1}$)	References
Ag-Fe_2O_3 microboxes	3 mg	5.0	4.67×10^{-3}	1.6	31	[54]
Ag-Fe_2O_3	10 mg	5.0	2.08×10^{-2}	2.1	42	[55]
Ag-SiO_2	10 mg	5.0	1.48×10^{-2}	1.5	30	[55]
Fe_3O_4@SiO_2–Ag	1 mg	3.7	4.00×10^{-3}	4.0	108	[56]
Fe_3O_4@SiO_2–Ag	1 mg	8.89	7.67×10^{-3}	7.67	86	[36]
Ag/KCC-1	0.2 mg	8.97	1.00×10^{-2}	50	557	[13]
Ag NPs@MWCNTs polymer composite	10 mg	0.25	7.88×10^{-3}	11.6	315	[57]
Cu-Ag/GP	10 mg	44.4	4.05×10^{-3}	0.4	1	[58]
Au-Ag bimetallic NPs supported on LDH	20 µl/1 mg	N/A	4.75×10^{-4}	23.8	N/A	[59]
Ag–γ-Fe_2O_3	0.1 mg	4.8[c]	6.92×10^{-3}	69.2	1442	This work

[a]The total mass of the catalyst was considered

[b]Only the mass of the metal(s) in the catalyst was considered

[c]Determined by ICP-OES

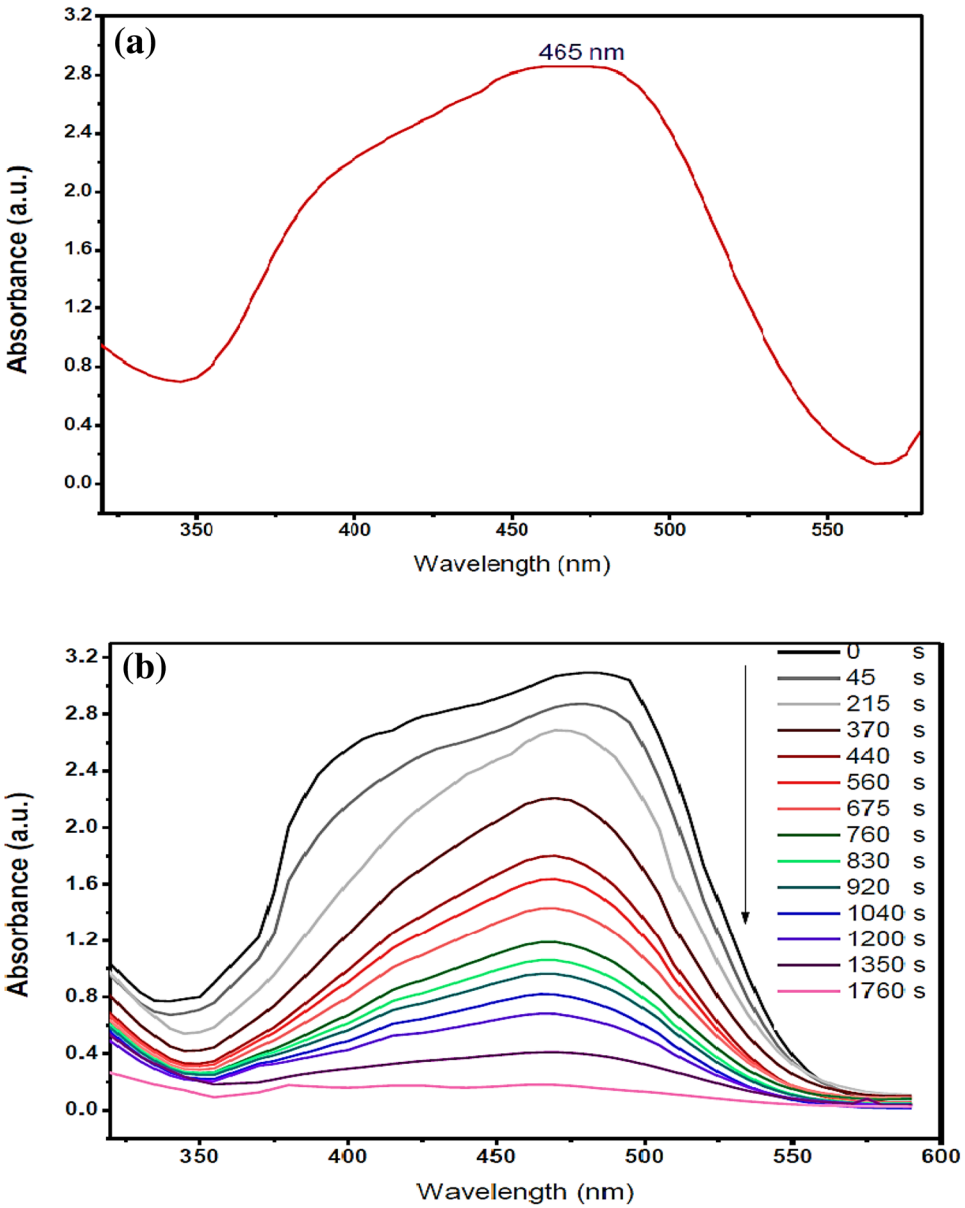

Fig. 10 The UV–Vis. spectra for: **a** MO and $NaBH_4$ before adding the catalyst, **b** successive degradation of MO after adding Ag–γ-Fe_2O_3 nanocomposite at 25 °C

less than 30 min. It is obvious that the catalytic activity and efficiency of the synthesized Ag–γ-Fe_2O_3 nanocomposite in the catalytic degradation of MO are significantly higher than these reported nanoparticles, with magnetic behavior advantage.

4 Conclusion

Ag–γ-Fe_2O_3 nanocomposite with superparamagnetic behavior and superior activity was synthesized. The synthesized Ag–γ-Fe_2O_3 nanocomposite exhibited superior catalytic activity for the reduction of NACs (4-NP and 2-NA) in the presence of $NaBH_4$. Besides, it showed a superior activity and high efficiency for the catalytic degradation of MO in the presence of $NaBH_4$. Moreover, Ag–γ-Fe_2O_3 nanocomposite was recycled for twelve times in the reduction of 4-NP as a model reaction and showed promising recycling results. Ag–γ-Fe_2O_3 nanocomposite provides an efficient simple scheme for the synthesis of other magnetic-based transition metal nanocomposites with superior activity and easy separation from the reaction mixture. These separable magnetically-based transition metal nanocomposites are highly efficient in numerous catalytic reduction reactions.

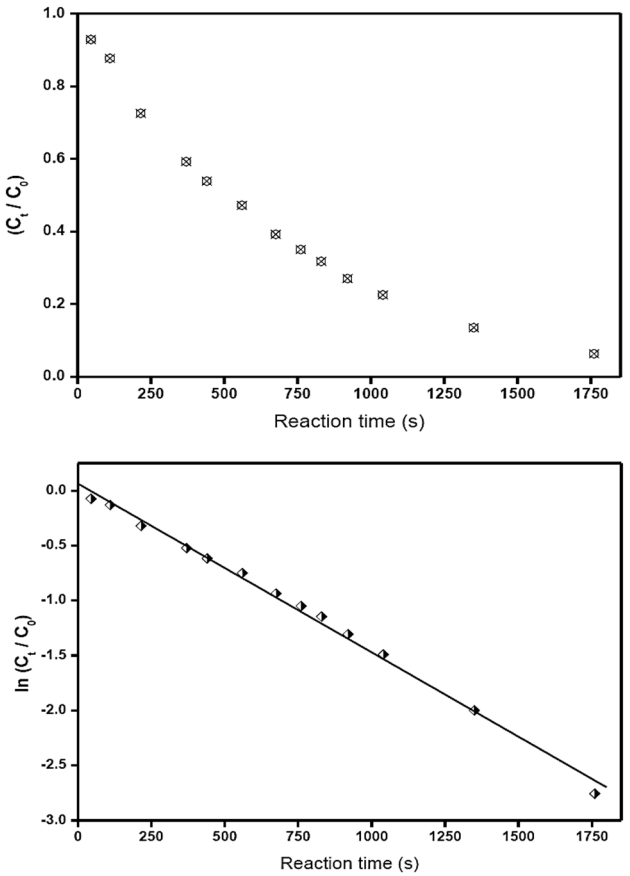

Fig. 11 Plots of (C_t/C_0) and $\ln(C_t/C_0)$ versus reaction time for catalytic degradation of MO in the presence of Ag–γ-Fe_2O_3 nanocomposite at 25 °C

Table 3 Comparison of catalytic activity of Ag–γ-Fe_2O_3 for the degradation of MO with reported catalysts

Catalyst	Decolorization efficiency (%)	Period time (min)	References
Au nanoparticles	≤40	40	[60]
Pt nanoparticles	≤40	40	[60]
MWCNT/TiO_2	93	100	[62]
MWCNTs	84.87	60	[63]
MWCNTs/Pd	99.31	60	[63]
Palladium/hydroxyapatite/Fe_3O_4 nanoparticles	≥95	200	[64]
Ag–γ-Fe_2O_3 nanocomposite	≥99	29.3	This work

Compliance with Ethical Standards

Conflict of interest We declare that no conflict of interest exists.

References

1. Barman BK, Nanda KK (2015) Rapid reduction of GO by hydrogen spill-over mechanism by in situ generated nanoparticles at room temperature and their catalytic performance towards 4-nitrophenol reduction and ethanol oxidation. Appl Catal A 491:45–51
2. Zhang J, Chen G, Chaker M, Rosei F, Ma D (2013) Gold nanoparticle decorated ceria nanotubes with significantly high catalytic activity for the reduction of nitrophenol and mechanism study. Appl Catal B 132:107–115
3. Evangelista V, Acosta B, Miridonov S, Smolentseva E, Fuentes S, Simakov A (2015) Highly active Au-CeO2@ZrO2 yolk–shell nanoreactors for the reduction of 4-nitrophenol to 4-aminophenol. Appl Catal B 166–167:518–528
4. Petrova B, Budinova T, Tsyntsarski B, Kochkodan V, Shkavro Z, Petrov N (2010) Removal of aromatic hydrocarbons from water by activated carbon from apricot stones. Chem Eng J 165(1):258–264
5. Shen X-E, Shan X-Q, Dong D-M, Hua X-Y, Owens G (2009) Kinetics and thermodynamics of sorption of nitroaromatic compounds to as-grown and oxidized multiwalled carbon nanotubes. J Colloid Interface Sci 330(1):1–8
6. Ren M, Song Y, Xiao S, Zeng P, Peng J (2011) Treatment of berberine hydrochloride wastewater by using pulse electro-coagulation process with Fe electrode. Chem Eng J 169(1):84–90
7. Zhao L, Zhao H (2018) Magnetic N-doped Co-carbon composites derived from metal organic frameworks as highly efficient catalysts for 4-nitrophenol reduction reaction. Dalton Trans 47:3321–3328
8. Chakrabarti S, Ganguli D, Chaudhuri S (2004) Optical properties of γ-Fe_2O_3 nanoparticles dispersed on sol–gel silica spheres. Physica E 24(3):333–342
9. Ichiyanagi Y, Kimishima Y (2002) Structural, magnetic and thermal characterizations of Fe_2O_3 nanoparticle systems. J Thermal Anal Calorim 69(3):919–923
10. Ye X, Lin D, Jiao Z, Zhang L (1998) The thermal stability of nanocrystalline maghemite. J Phys D 31(20):2739
11. Innocenzi P (2003) Infrared spectroscopy of sol–gel derived silica-based films: a spectra-microstructure overview. J Non-Cryst Solids 316(2):309–319
12. Theivasanthi T, Alagar M (2011) Electrolytic synthesis and characterizations of silver nanopowder. arXiv preprint arXiv:1111.0260.
13. Dong Z, Le X, Li X, Zhang W, Dong C, Ma J (2014) Silver nanoparticles immobilized on fibrous nano-silica as highly efficient and recyclable heterogeneous catalyst for reduction of 4-nitrophenol and 2-nitroaniline. Appl Catal B 158:129–135
14. Moon B-H, Park Y-B, Park K-H (2011) Fenton oxidation of orange II by pre-reduction using nanoscale zero-valent iron. Desalination 268(1–3):249–252
15. Park H, Choi W (2003) Visible light and Fe (III)-mediated degradation of acid orange 7 in the absence of H_2O_2. J Photochem Photobiol A 159(3):241–247
16. Devi LG, Kumar SG, Reddy KM, Munikrishnappa C (2009) Photo degradation of methyl orange an azo dye by advanced fenton process using zero valent metallic iron: Influence of various reaction parameters and its degradation mechanism. J Hazard Mater 164(2–3):459–467
17. Li X, Xue H, Pang H (2017) Facile synthesis and shape evolution of well-defined phosphotungstic acid potassium nanocrystals as a highly efficient visible-light-driven photocatalyst. Nanoscale 9(1):216–222

18. Taylor R, Coulombe S, Otanicar T, Phelan P, Gunawan A, Lv W et al (2013) Small particles, big impacts: a review of the diverse applications of nanofluids. J Appl Phys 113(1):011301
19. Ó Dálaigh C, Corr SA, Gun'ko Y, Connon SJ (2007) A magnetic-nanoparticle-supported 4-N, N-dialkylaminopyridine catalyst: excellent reactivity combined with facile catalyst recovery and recyclability. Angew Chem 119(23):4407–4410
20. Frey NA, Peng S, Cheng K, Sun S (2009) Magnetic nanoparticles: synthesis, functionalization, and applications in bioimaging and magnetic energy storage. Chem Soc Rev 38(9):2532–2542
21. Singamaneni S, Bliznyuk VN, Binek C, Tsymbal EY (2011) Magnetic nanoparticles: recent advances in synthesis, self-assembly and applications. J Mater Chem 21(42):16819–16845
22. Li D, Teoh WY, Selomulya C, Woodward RC, Amal R, Rosche B (2006) Flame-sprayed superparamagnetic bare and silica-coated maghemite nanoparticles: synthesis, characterization, and protein adsorption-desorption. Chem Mater 18(26):6403–6413
23. Pankhurst QA, Connolly J, Jones S, Dobson J (2003) Applications of magnetic nanoparticles in biomedicine. J Phys D 36(13):R167
24. Lévy M, Wilhelm C, Siaugue J-M, Horner O, Bacri J-C, Gazeau F (2008) Magnetically induced hyperthermia: size-dependent heating power of γ-Fe_2O_3 nanoparticles. J Phys 20(20):204133
25. Kolhatkar AG, Jamison AC, Litvinov D, Willson RC, Lee TR (2013) Tuning the magnetic properties of nanoparticles. Int J Mol Sci 14(8):15977–16009
26. Thomas R, Park I-K, Jeong YY (2013) Magnetic iron oxide nanoparticles for multimodal imaging and therapy of cancer. Int J Mol Sci 14(8):15910–15930
27. Berry CC, Curtis AS (2003) Functionalisation of magnetic nanoparticles for applications in biomedicine. J Phys D 36(13):R198
28. Huo L, Li W, Lu L, Cui H, Xi S, Wang J et al (2000) Preparation, structure, and properties of three-dimensional ordered α-Fe_2O_3 nanoparticulate film. Chem Mater 12(3):790–794
29. Suresh R, Prabu R, Vijayaraj A, Giribabu K, Stephen A, Narayanan V (2012) Facile synthesis of cobalt doped hematite nanospheres: magnetic and their electrochemical sensing properties. Mater Chem Phys 134(2):590–596
30. Biswal RC (2011) Pure and Pt-loaded gamma iron oxide as sensor for detection of sub ppm level of acetone. Sens Actuators B 157(1):183–188
31. Jing Z (2006) Fabrication and gas sensing properties of Ni-doped gamma-Fe_2O_3 by anhydrous solvent method. Mater Lett 60(28):3315–3318
32. Barroso M, Cowan AJ, Pendlebury SR, Grätzel M, Klug DR, Durrant JR (2011) The role of cobalt phosphate in enhancing the photocatalytic activity of α-Fe_2O_3 toward water oxidation. J Am Chem Soc 133(38):14868–14871
33. Darezereshki E (2011) One-step synthesis of hematite (α-Fe_2O_3) nano-particles by direct thermal-decomposition of maghemite. Mater Lett 65(4):642–645
34. Rocher V, Manerova J, Kinnear M, Evans DJ, Francesconi MG (2014) Direct amine-functionalisation of gamma-Fe_2O_3 nanoparticles. Dalton Trans 43(7):2948–2952
35. Xu YX, Li B, Zheng SS, Wu P, Zhang J, Xue H et al (2018) Ultrathin two-dimensional cobalt-organic framework nanosheets for high-performance electrocatalytic oxygen evolution. J Mater Chem A. https://doi.org/10.1039/C8TA03128B
36. Chi Y, Yuan Q, Li Y, Tu J, Zhao L, Li N et al (2012) Synthesis of Fe_3O_4@ SiO_2–Ag magnetic nanocomposite based on small-sized and highly dispersed silver nanoparticles for catalytic reduction of 4-nitrophenol. J Colloid Interface Sci 383(1):96–102
37. Cheng K, He Y, Miao Y, Zou B, Wang Y, Wang T et al (2006) Quantum size effect on surface photovoltage spectra: alpha-Fe_2O_3 nanocrystals on the surface of monodispersed silica microsphere. J Phys Chem B 110(14):7259–7264
38. Banerjee A, Patra S, Chakrabarti M, Sanyal D, Pal M, Pradhan SK (2011) Microstructure, Mössbauer, and optical characterizations of nanocrystalline α-Fe_2O_3 synthesized by chemical route. ISRN Ceram. https://doi.org/10.5402/2011/406094
39. Li X, Wang X, Song S, Liu D, Zhang H (2012) Selectively deposited noble metal nanoparticles on Fe_3O_4/graphene composites: stable, recyclable, and magnetically separable catalysts. Chemistry 18(24):7601–7607
40. Gu H, Wang J, Ji Y, Wang Z, Chen W, Xue G (2013) Facile and controllable fabrication of gold nanoparticles-immobilized hollow silica particles and their high catalytic activity. J Mater Chem A 1(40):12471–12477
41. Pradhan N, Pal A, Pal T (2001) Catalytic reduction of aromatic nitro compounds by coinage metal nanoparticles. Langmuir 17(5):1800–1802
42. Gu Y, Jiao Y, Zhou X, Wu A, Buhe B, Fu H (2018) Strongly coupled Ag/TiO_2 heterojunctions for effective and stable photothermal catalytic reduction of 4-nitrophenol. Nano Res 11(1):126–141
43. Baruah B, Gabriel GJ, Akbashev MJ, Booher ME (2013) Facile synthesis of silver nanoparticles stabilized by cationic polynorbornenes and their catalytic activity in 4-nitrophenol reduction. Langmuir 29(13):4225–4234
44. Fath RH, Hoseini SJ, Khozestan HG (2017) A nanohybrid of organoplatinum(II) complex and graphene oxide as catalyst for reduction of p-nitrophenol. J Organomet Chem 842:1–8
45. Arumugam V, Sriram P, Yen T-J, Redhi GG, Gengan RM (2018) Nano-material as an excellent catalyst for reducing a series of nitroanilines and dyes: triphosphonated ionic liquid-$CuFe_2O_4$-modified boron nitride. Appl Catal B 222:99–114
46. Sahiner N, Ozay H, Ozay O, Aktas N (2010) New catalytic route: hydrogels as templates and reactors for in situ Ni nanoparticle synthesis and usage in the reduction of 2-and 4-nitrophenols. Appl Catal A 385(1):201–207
47. Sahiner N, Ozay O (2012) Enhanced catalytic activity in the reduction of 4-nitrophenol and 2-nitrophenol by p (AMPS)-Cu (0) hydrogel composite materials. Curr Nanosci 8(3):367–374
48. Sahiner N, Ozay H, Ozay O, Aktas N (2010) A soft hydrogel reactor for cobalt nanoparticle preparation and use in the reduction of nitrophenols. Appl Catal B 101(1):137–143
49. Yang S, Nie C, Liu H, Liu H (2013) Facile synthesis and catalytic application of Ag–Fe_2O_3–carbons nanocomposites. Mater Lett 100:296–298
50. Tang S, Vongehr S, Meng X (2009) Carbon spheres with controllable silver nanoparticle doping. J Phys Chem C 114(2):977–982
51. Rashid MH, Mandal TK (2007) Synthesis and catalytic application of nanostructured silver dendrites. J Phys Chem C 111(45):16750–16760
52. Gao C, An Q, Xiao Z, Zhai S, Zhai B, Shi Z (2018) Alginate and polyethyleneimine dually mediated synthesis of nanosilver-containing composites for efficient p-nitrophenol reduction. Carbohydr Polym 181:744–751
53. Sau TK, Pal A, Pal T (2001) Size regime dependent catalysis by gold nanoparticles for the reduction of eosin. J Phys Chem B 105(38):9266–9272
54. Jiang Z, Jiang D, Hossain AS, Qian K, Xie J (2015) In situ synthesis of silver supported nanoporous iron oxide microbox hybrids from metal-organic frameworks and their catalytic application in p-nitrophenol reduction. Phys Chem Chem Phys 17(4):2550–2559
55. Feng J, Fan D, Wang Q, Ma L, Wei W, Xie J et al (2017) Facile synthesis silver nanoparticles on different xerogel supports as highly efficient catalysts for the reduction of p-nitrophenol. Colloids Surf A 520:743–756
56. Du X, He J, Zhu J, Sun L, An S (2012) Ag-deposited silica-coated Fe_3O_4 magnetic nanoparticles catalyzed reduction of p-nitrophenol. Appl Surf Sci 258(7):2717–2723

57. Alshehri SM, Almuqati T, Almuqati N, Al-Farraj E, Alhokbany N, Ahamad T (2016) Chitosan based polymer matrix with silver nanoparticles decorated multiwalled carbon nanotubes for catalytic reduction of 4-nitrophenol. Carbohydr Polym 151:135–143
58. Ismail M, Khan M, Khan SB, Khan MA, Akhtar K, Asiri AM (2018) Green synthesis of plant supported CuAg and CuNi bimetallic nanoparticles in the reduction of nitrophenols and organic dyes for water treatment. J Mol Liq 260:78–91
59. Arora N, Mehta A, Mishra A, Basu S (2018) 4-Nitrophenol reduction catalysed by Au-Ag bimetallic nanoparticles supported on LDH: homogeneous vs. heterogeneous catalysis. Appl Clay Sci 151:1–9
60. Gupta N, Singh HP, Sharma RK (2011) Metal nanoparticles with high catalytic activity in degradation of methyl orange: an electron relay effect. J Mol Catal A 335(1):248–252
61. Naraginti S, Stephen FB, Radhakrishnan A, Sivakumar A (2015) Zirconium and silver co-doped TiO_2 nanoparticles as visible light catalyst for reduction of 4-nitrophenol, degradation of methyl orange and methylene blue. Spectrochim Acta A 135:814–819
62. Saleh TA, Gupta VK (2012) Photo-catalyzed degradation of hazardous dye methyl orange by use of a composite catalyst consisting of multi-walled carbon nanotubes and titanium dioxide. J Colloid Interface Sci 371(1):101–106
63. Cano OA, González CR, Paz JH, Madrid PA, Casillas PG, Hernández AM et al (2017) Catalytic activity of palladium nanocubes/multiwalled carbon nanotubes structures for methyl orange dye removal. Catal Today 282:168–173
64. Safavi A, Momeni S (2012) Highly efficient degradation of azo dyes by palladium/hydroxyapatite/Fe_3O_4 nanocatalyst. J Hazard Mater 201:125–131